Available online at www.sciencedirect.com
ScienceDirect
Trans. Nonferrous Met. Soc. China 33(2023) 2970−2985
Transactions of Nonferrous Metals Society of China
www.tnmsc.cn

Statistical investigation of deformation mechanisms in rolled Mg sheet during compression

Dong-di YIN[1], Bo CHEN[1], Yan-qin CHAI[1], You-fu WAN[1], Hao ZHOU[2], Jiang ZHENG[3], Qu-dong WANG[4], Ying ZENG[1]

1. Key Laboratory of Advanced Technologies of Materials, Ministry of Education, School of Materials Science and Engineering, Southwest Jiaotong University, Chengdu 610031, China;
2. Nano and Heterogeneous Materials Center, School of Materials Science and Engineering, Nanjing University of Science and Technology, Nanjing 210094, China;
3. International Joint Laboratory for Light Alloys (Ministry of Education), College of Materials Science and Engineering, Shenyang National Laboratory for Materials Science, Chongqing University, Chongqing 400044, China;
4. National Engineering Research Center of Light Alloys Net Forming, School of Materials Science and Engineering, Shanghai Jiao Tong University, Shanghai 200240, China

Received 7 April 2022; accepted 22 September 2022

Abstract: A statistical investigation of the operating slip/twinning modes and their interactions at grain scale over a large area, containing ~400 grains, was carried out on rolled Mg sheets during room-temperature compression based on EBSD and slip trace analysis. For 10% strain, the slip mode was dominated by basal slip (89%). All the 363 identified twins were tension twins. The concave-up stress−strain curve indicated a twinning-dominated deformation behavior, which was further confirmed by the large twinned area fraction (41%) after the deformation. Most twin variants (79%) followed the Schmid law. The Luster−Morris parameter (m') did not correlate well to twin transmission. However, most twin transmissions (82%) exhibited larger normalized m (Schmid factor) and m' values. Additional slip systems were frequently active in the twin domains while not in the parent, which can be explained by Schmid law. Slip transfer across the twin boundaries was also observed. Statistical m analysis revealed that twinning activity was closely related to prismatic slip.

Key words: Mg; EBSD; slip trace analysis; twin variant selection; slip−twinning interaction

1 Introduction

Magnesium (Mg) alloys have excellent weight reduction potential in transportation and aerospace fields, due to their low density and high specific strength [1−6]. However, the low symmetry of the hexagonal close-packed (HCP) crystal structure and significant plastic anisotropy of Mg alloys lead to limited plasticity and formability at room temperature [7−9], which prevents their widespread applications.

The common slip modes in Mg and its alloys include basal $\langle a \rangle$ slip, prismatic $\langle a \rangle$ slip, and pyramidal II $\langle c+a \rangle$ slip [10]. Among them, only pyramidal II $\langle c+a \rangle$ slip can coordinate the c-axis deformation and provide five independent slip systems. What's more, the critical resolved shear stress (CRSS) values for individual slip modes exhibit a significant disparity. For example, the

Corresponding author: Dong-di YIN, Tel: +86-28-87634673, E-mail: ahnydd@swjtu.edu.cn; Ying ZENG, E-mail: clzy@home.swjtu.edu.cn
DOI: 10.1016/S1003-6326(23)66311-3

$CRSS_{non\text{-}basal}/CRSS_{basal}$ can be as high as 100 at room temperature [11]. Thus, the non-basal slip modes are hard to be activated at room temperature. Deformation twinning, as an additional deformation mode besides slip, can coordinate the *c*-axis deformation [12−14], but its strain contribution is limited [15]. $\{10\bar{1}2\}\langle\bar{1}011\rangle$ tension twin (TTW) and $\{10\bar{1}1\}\langle10\bar{1}\bar{2}\rangle$ contraction twin (CTW) are two common twinning modes in Mg [10]. However, twins exhibit polarity, i.e., only if the crystal *c*-axis is subjected to tensile stress the TTW can be activated, while the opposite is true for the CTW [10]. Since the CRSS of CTW is considerably larger than that of TTW, the CTW is hardly activated. The above plastic deformation modes determine the complex mechanical behavior of Mg and its alloys. Therefore, detailed information on slip/twinning activity is essential for understanding the plasticity of Mg and its alloys.

Several methodologies are available for evaluating the slip activity experimentally. The transmission electron microscopy (TEM) is one of the widely used methodologies that can directly demonstrate the presence of dislocations but suffers from a lack of statistics. For example, a typical TEM dislocation analysis is usually performed on less than 10 grains [8,16−19]. What's more, it is well-accepted that the plastic deformation of Mg is highly heterogeneous at various length scales [20,21]. Therefore, statistical analysis of the deformation mechanisms of Mg, which is performed in the present study, is essential. Slip trace analysis [21−24] is a powerful technique to solve the above problem. This technique has recently been successfully used to investigate slip activity in Mg and its alloys [21−25]. Besides dislocation slip, twinning is also an essential deformation mechanism for Mg [26]. Understanding twinning activity and variant selection based on statistical analysis are also critical [22,26,27]. It is worth noting that most studies were focused on the deformation mechanism of Mg under tension [26,28−30]. However, a significant tensile−compression asymmetry exists in Mg [24,31]. Therefore, a quantitative and statistical investigation on individual slip and twinning activities of Mg during compression is needed.

In this work, a quantitative and statistical investigation of deformation mechanisms for rolled Mg sheets at grain scale over a large area, which contains ~400 grains, was performed based on EBSD and slip trace analysis. The slip/twinning activities were analyzed in detail, including quantitative information on individual slip modes, twin variants, slip transfer, twin transmission, etc. In addition, the observed interactions between slip and twinning, such as slip transfer across twin boundaries and slip activated within the twin domains, were analyzed, which has scientific importance for further understanding the complex interactions of deformation mechanisms for Mg. This work provides a detailed analysis of the deformation mechanism during compression and a profound understanding of the slip/twinning activity and their interactions in Mg. The new insights revealed by the present work are helpful for further understanding the complex deformation behavior of Mg, as well as valuable for validation and improvement of advanced crystal plasticity modelling.

2 Experimental

The high-purity Mg (99.9 wt.%) sheets, were prepared by multiple-pass hot rolling and then annealing at 350 °C for 25 s. Microstructure and crystallographic orientation data were obtained by a JEOL JSM−7800F field emission scanning electron microscope (SEM) with an Oxford Instrument Nordlys Nano electron backscatter diffraction (EBSD) detector. The observation plane was always the RD−TD plane, which contained the rolling direction (RD) and the transverse direction (TD). The sample surfaces for SEM/EBSD observations were mechanically polished, followed by chemical polishing and then etching.

The rectangular compression specimens with dimensions of 5 mm × 5 mm × 7.5 mm (width × thickness × length) were obtained using electrical spark machining. The RD and TD were parallel to the length and width, respectively. Compression tests with an initial strain rate of 1×10^{-3} s^{-1} were performed along the RD using an MTS−CMT5105 universal tester. Three tests were repeated for accuracy and reproducibility.

The quasi-in-situ compression experiments, interrupted at 5% and 10% strain, were performed to investigate the microstructure evolution on the specimen surface during deformation. Subsequently, the deformation characteristics of the same area in the center of the sample were analyzed by SEM and EBSD. The selected area contains more than 400

grains to ensure statistics. The working parameters of EBSD were as follows: accelerating voltage of 20 kV and working distance of 15 mm. In addition, the sample was tilted by 70° and the step size was 0.5 μm. The raw EBSD data were analyzed by the home-made MATLAB code based on the MTEX toolbox [32]. Details of the slip trace analysis and twin variant identification techniques can be found in our previous works [24,26].

3 Results

3.1 Initial microstructure

The representative microstructure of the rolled Mg sheet on the RD−TD plane is shown in Fig. 1. As can be seen in Figs. 1(a−c), the microstructure exhibited uniform equiaxed grains with an average grain size of (12.9±7.9) μm. The {0001} pole figure (PF) for ND and the inverse pole figure (IPF) along the RD are presented in Fig. 1(d). A strong basal texture, as revealed by the {0001} PF, with a maximum intensity of 14 multiples random distribution (mrd), indicated that the *c*-axis of most grains was nearly parallel to the ND. The maximum pole of the IPF appears between $\langle 11\bar{2}0 \rangle$ and $\langle 10\bar{1}0 \rangle$ with an intensity of 2.2 mrd.

3.2 Mechanical behavior

Figure 2(a) illustrates the engineering stress−engineering plastic strain curve of rolled Mg sheet during compression along RD. A sigmoidal characteristic (concave-up) of the compression curve was observed, which was related to the twinning-dominated deformation mechanism [22]. The compressive yield strength (CYS), ultimate compressive strength (UCS), and uniform compressive elongation (CEL) of Mg were (52±3) MPa, (273±2) MPa and (11.8±0.2)%, respectively. Figure 2(b) shows the strain hardening rate curve, exhibiting a feature of rapid decrease followed by a remarkable increase and finally a gradual decrease, which corresponds to the sigmoidal shape engineering stress−engineering plastic strain curve in Fig. 2(a).

3.3 General microstructural evolution

Figure 3 illustrates the representative microstructural evolution in the same area during quasi-in-situ compression. Figure 3(a) shows the microstructure before loading, which exhibited no deformation features. The slip traces were observed in one grain after 5% strain, as shown in Fig. 3(b). With increasing the strain to 10%, many twins and

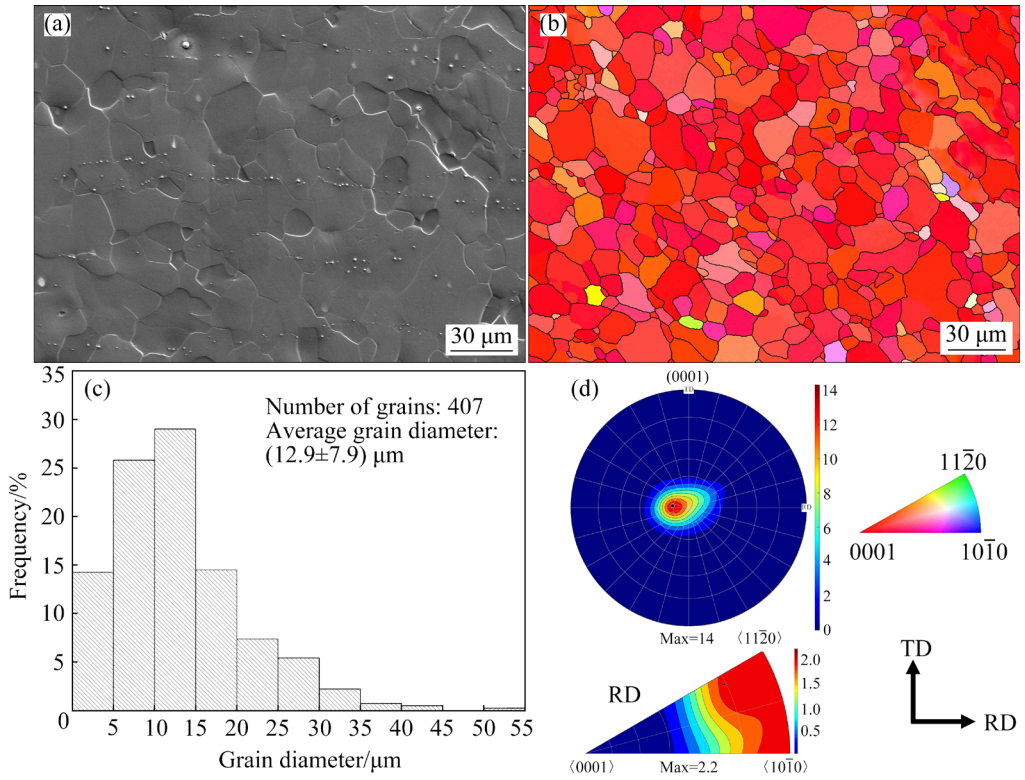

Fig. 1 Initial microstructure of rolled Mg sheet for RD−TD plane: (a) SEM photomicrograph; (b) EBSD IPF along ND; (c) Distribution of equivalent grain diameter; (d) {0001} PF for ND and IPF along RD

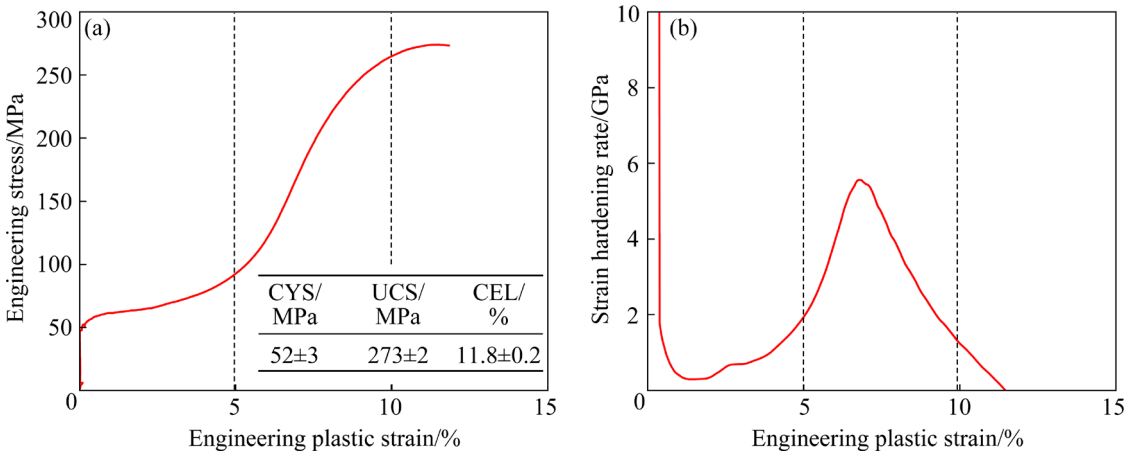

Fig. 2 Compressive mechanical behavior curves along RD: (a) Engineering stress−engineering plastic strain curve (The compressive mechanical properties are inserted); (b) Strain hardening rate curve (The quasi-in-situ experiment was interrupted at 5% and 10% strain, as marked by the dashed line)

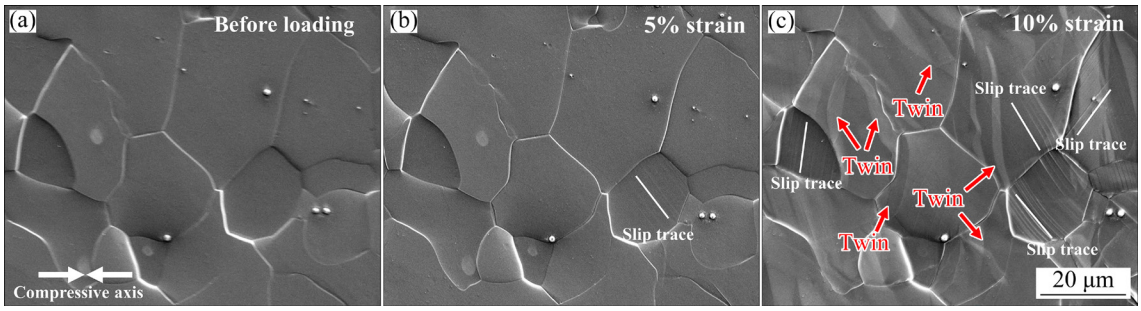

Fig. 3 Sequential SE SEM photomicrographs showing microstructural evolution of Mg during quasi-in-situ compression deformation along RD: (a) Before loading; (b) After 5% strain; (c) After 10% strain (The twins and slip traces are indicated by red arrows and white solid lines, respectively)

slip traces appeared, as indicated by red arrows and white solid lines. The slip traces exhibited typical planar slip characteristics, and only one set of parallel slip traces existed in one grain, indicating that the slip was dominated by single slip.

3.4 Slip activity

Slip trace analysis was used to identify the active slip systems corresponding to the observed slip traces. All possible theoretical slip traces and Schmid factor (m) corresponding to the slip system were calculated based on grain average orientation and loading direction. The slip systems were identified according to the deviation angle between the theoretical and observed slip traces. Three slip modes, including 12 slip systems, were considered in this study [24]: $\langle 11\bar{2}0\rangle\{0001\}$ basal $\langle a\rangle$ slip, $\langle 11\bar{2}0\rangle\{10\bar{1}0\}$ prismatic $\langle a\rangle$ slip, and $\langle \bar{1}\bar{1}23\rangle$-$\{11\bar{2}2\}$ pyramidal II $\langle c+a\rangle$ slip.

Figure 4 shows an illustration of slip trace identification in Grain 278 after 10% plastic strain. A set of slip traces (marked by the blue solid line) was observed in Grain 278 (Fig. 4(a)). Figure 4(c) presents the theoretical slip traces and the corresponding m, which can be obtained by inputting the EBSD date (Euler angles) before deformation (Fig. 4(b)) into the home-made MATLAB code. In Grain 278, the prismatic $\langle a\rangle$ slip 4-$(0\bar{1}10)[2\bar{1}\bar{1}0]$ with the smallest deviation angle (1°) was identified as the activated slip system. The corresponding crystallographic information, including the slip plane and direction of the identified slip system, was provided in the unit cell. For slip systems sharing the same slip plane, such as the basal $\langle a\rangle$ slip, the slip system with the largest m was considered to be the activated slip system.

A total of 90 slip traces observed in 407 grains were identified using the above slip trace analysis. Figure 5 presents the frequency of individual slip

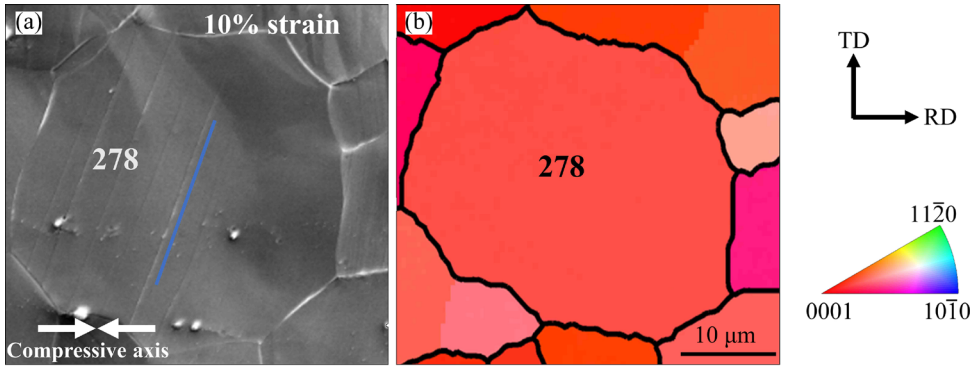

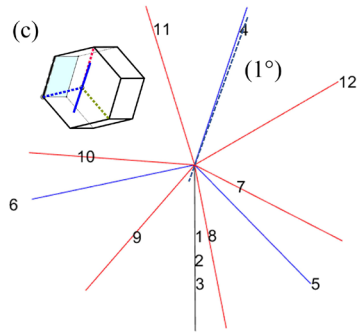

No.	Slip system		Schmid factor
1	Basal ⟨*a*⟩	(0001)[2$\bar{1}\bar{1}$0]	0.09
2		(0001)[$\bar{1}$2$\bar{1}$0]	0.21
3		(0001)[$\bar{1}\bar{1}$20]	0.31
4	Prismatic ⟨*a*⟩	(0$\bar{1}$10)[2$\bar{1}\bar{1}$0]	0.25
5		(10$\bar{1}$0)[$\bar{1}$2$\bar{1}$0]	0.44
6		($\bar{1}$100)[$\bar{1}\bar{1}$20]	0.19
7	Pyramidal II ⟨*c*+*a*⟩	(2$\bar{1}\bar{1}$2)[$\bar{1}$223]	0.05
8		(11$\bar{2}$2)[$\bar{1}\bar{1}$23]	0.18
9		($\bar{1}$2$\bar{1}$2)[1$\bar{2}$13]	0.03
10		($\bar{2}$112)[2$\bar{1}\bar{1}$3]	0.02
11		($\bar{1}\bar{1}$22)[11$\bar{2}$3]	0.46
12		(1$\bar{2}$12)[$\bar{1}$2$\bar{1}$3]	0.22

Fig. 4 Illustration of slip traces identification in Grain 278 after 10% strain: (a) SEM photomicrograph of Grain 278; (b) IPF map before loading; (c) Possible slip system trace calculated by grain Euler angle and corresponding Schmid factor

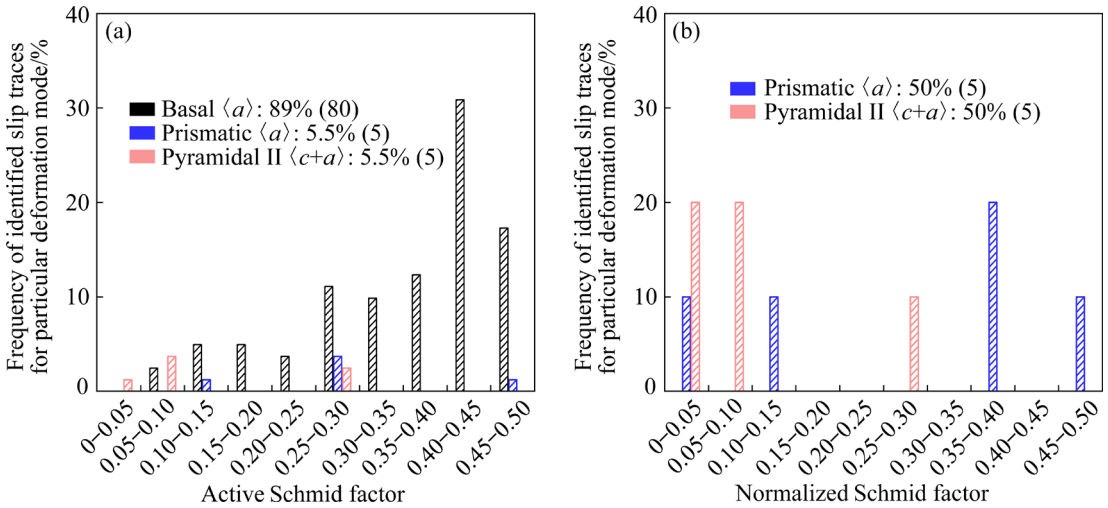

Fig. 5 Frequency of identified slip traces for particular deformation mode and distribution of Schmid factor (m) (a) and normalized Schmid factor (m_{nor}) (b) at 10% strain

modes and the distribution of the Schmid factors. As can be seen in Fig. 5(a), basal ⟨*a*⟩ slip had the highest percentage (89%), while both prismatic ⟨*a*⟩ slip and pyramidal II ⟨*c*+*a*⟩ slip was 5.5%. For basal slip, 83% of the m values were greater than 0.25. However, 50% of non-basal slips exhibited the m values less than 0.25. Considering that the theoretical maximum m (m_{max}) values for non-basal slip might be comparatively low, a normalized Schmid factor (m_{nor}) was defined to evaluate the proximity of m to the theoretical m_{max}, and the equation is as follows [21−24]:

$$m_{nor}=\frac{m-m_{min}}{2(m_{max}-m_{min})} \quad (1)$$

where m_{max} and m_{min} represent the maximum and minimum Schmid factors for a particular slip mode, respectively [21]. After normalizing the m of non-basal slip by Eq. (1), as seen in Fig. 5(b), there were still 60% of m_{nor} values less than 0.2, indicating that the activated non-basal slips exhibited no-Schmid behavior.

Slip transfer, an important mechanism for coordinating intergranular deformation [21], was observed in the present study. The Luster−Morris parameter (m') was used to assess the likelihood of the slip transfer, calculated by the following equation [21−25]:

$$m'=\cos\kappa\cos\psi \tag{2}$$

where κ and ψ represent the angle of Burgers vectors and angle of slip plane normal of the two transferred slip systems, respectively. Higher m' values (close to 1) indicate better geometrical compatibility of the two slip systems, and the slip transfers are considered to be more likely to occur.

In the same way as Eq. (1), the normalization of m' is calculated as follows [21−23]:

$$m'_{nor}=\frac{m'-m'_{min}}{m'_{max}-m'_{min}} \tag{3}$$

The m'_{nor} was used to assess the closeness between m' and m'_{max} among all 144 possible transfer combinations with 12 slip systems considered in this study.

Five pairs of slip transfers were observed near the grain boundaries (GB), as presented in Fig. 6 and Table 1. It was found that slip transfers were observed between the same (Figs. 6(a, b)) or different (Figs. 6(c, d)) slip systems. For instance, as seen in Fig. 6(a), in Grain pair 329−334, the transferred slip systems were both basal $\langle a\rangle$ slip with m values of 0.43 and 0.42, respectively, and the corresponding m' and m'_{nor} exhibited larger values (greater than 0.8). The pyramidal II $\langle c+a\rangle$ slip and basal $\langle a\rangle$ slip transferred between Grain pair 233−245 (Fig. 6(d)), with relatively lower m' and m'_{nor} values (less than 0.4).

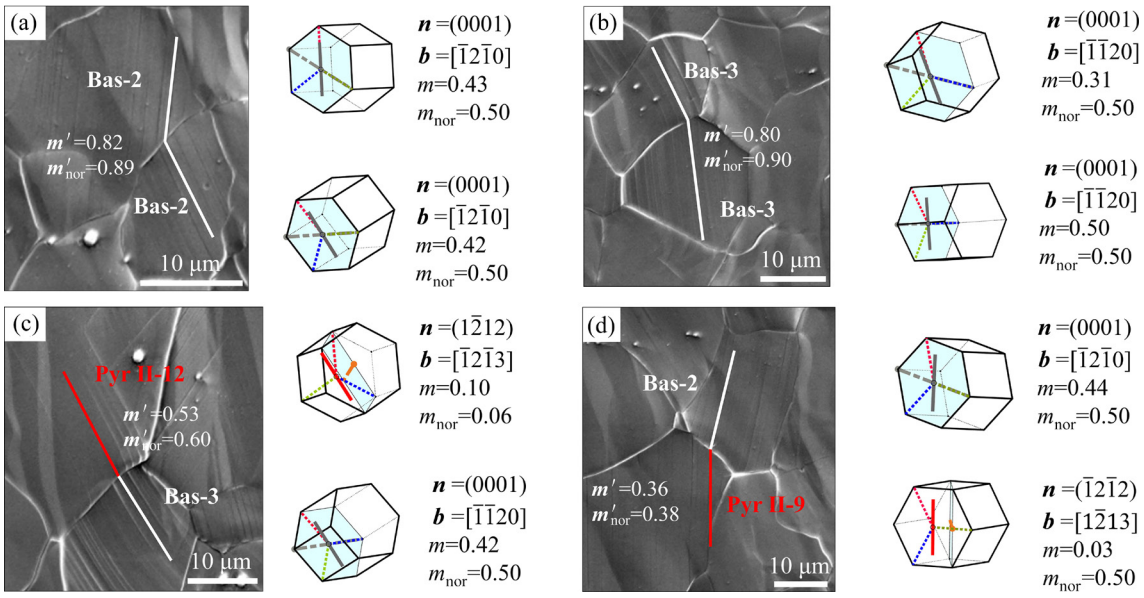

Fig. 6 SE SEM photomicrographs of representative slip transfers across GB at 10% strain (The slip systems of transferred pairs are visualized in the unit cells)

Table 1 Detailed information of slip transfer pairs at grain boundary for 10% strain

Grain ID	Deformation ratio/%	Slip transfer	m	m_{nor}	m'	m'_{nor}
70−86	10	Bas2−Bas2	0.34−0.41	0.5−0.5	0.68	0.35
189−202	10	Bas2−Bas2	0.31−0.5	0.5−0.5	0.80	0.9
329−334	10	Bas2−Bas2	0.43−0.42	0.5−0.5	0.82	0.89
233−245	10	Pyr II9−Bas2	0.03−0.44	0.5−0.5	0.36	0.38
134−139	10	Bas3−Pyr II12	0.42−0.1	0.5−0.06	0.53	0.6

Figure 7 illustrates the deviation angles between the observed and the best-matched theoretical slip traces for all 90 slip traces observed in this study. Most of the deviation angles (83%) were within 4°, and there were no deviation angles over 6°. The reason for the deviation between theoretical slip trace and real slip trace might be the lattice rotation during deformation and/or the misalignment of sample and SEM/EBSD systems.

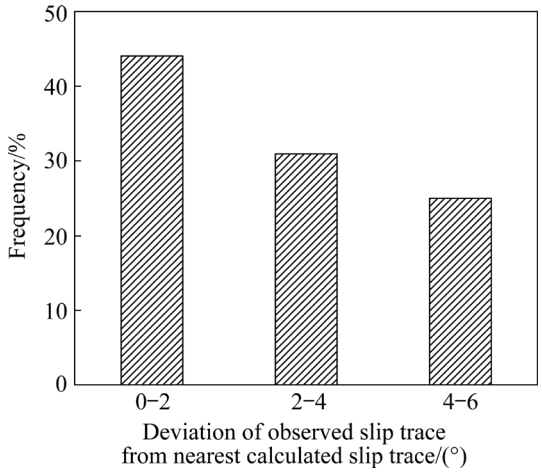

Fig. 7 Distribution of deviation angles between observed and best-matched slip traces

3.5 Twinning activity

Details of the twinning activity were analyzed after 10% strain based on EBSD data. The twinning activity analysis was carried out according to the twin boundary misorientation. Five twin modes were considered in this study, and the corresponding rotation axis/angle were as follows [22]: $\{10\bar{1}2\}$ tension twin (TTW): $\langle 1\bar{2}10\rangle$/86°; $\{10\bar{1}1\}$ contraction twin (CTW): $\langle 1\bar{2}10\rangle$/56°; $\{10\bar{1}3\}$ contraction twin (CTW): $\langle 1\bar{2}10\rangle$/64°; $\{10\bar{1}1\}$–$\{10\bar{1}2\}$ double twin (DTW): $\langle 1\bar{2}10\rangle$/38°; $\{10\bar{1}3\}$–$\{10\bar{1}2\}$ double twin (DTW): $\langle 1\bar{2}10\rangle$/22°.

The microstructure of Mg after 10% strain, including the IFP map along the ND, twin boundary identification and {0001}, $\{10\bar{1}0\}$ PF, is shown in Fig. 8. After 10% strain, a significant number of twin boundaries were identified, and all of them were $\{10\bar{1}2\}$ TTW boundaries, while no CTW or DTW boundaries were observed (Fig. 8(b)). As mentioned above, the TTW can cause the crystal to rotate by ~86° along the $\langle 1\bar{2}10\rangle$ axis. The {0001} PF before loading showed that the *c*-axis of most grains was nearly parallel to ND (Fig. 1(d)). After 10% strain, the *c*-axis of lots of grains tilted by ~90°

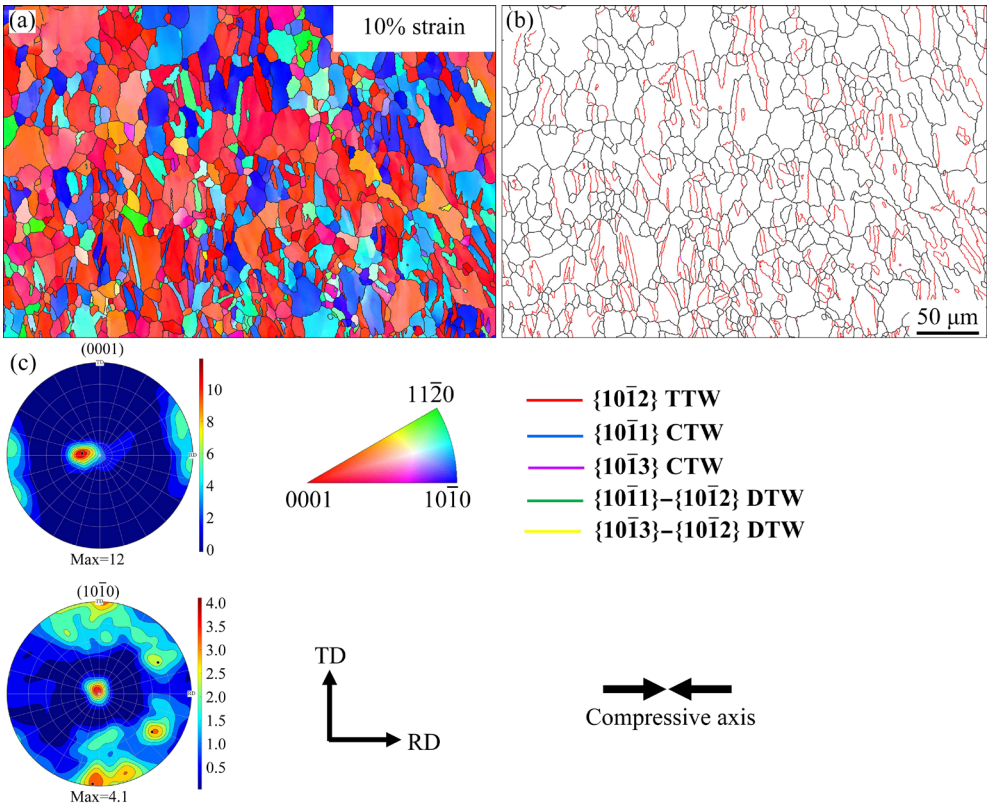

Fig. 8 Microstructure of Mg after 10% strain: (a) IPF map along ND; (b) Identified twin boundaries based on EBSD misorientation analysis for RD−TD plane; (c) {0001} and $\{10\bar{1}0\}$ PF map

from ND to RD (Fig. 8(c)), which was consistent with the significant TTW boundaries (Fig. 8(b)).

Since each parent grain has six crystallographically equivalent twinning planes (κ_1) and twinning directions (η_1), the TTW has six variants, designated as V1, V2, ⋯, V6 [22]. The orientation of the six theoretical twin variants can be calculated by inputting the EBSD data into the home-made MATLAB code. Subsequently, the activated twin variants were identified by the orientation deviation between the observed twin and the six theoretical variants. Figure 9 shows an example of the variant identification for Grain 315. Two TTWs were observed in Fig. 9(a), and the white solid line indicated the twin boundary. In Fig. 9(b), the first row shows the orientation of the parent grain 315 (labeled as 315-P). The orientations of theoretical twin variants and twins are presented in second and third rows, respectively, and the best-matched theoretical variants were selected as the activated one.

All TTWs were subjected to the twin variant analysis using the above method to further investigate the twin activation. A total of 363 twins were observed in 407 grains, and the detailed information on the twins is given in Table 2. The morphology of the TTWs, including area, width, thickness and true thickness, is shown in Fig. 10. The average twinned area was (110±185) μm^2, implying that some grains were extremely twinned. This is consistent with Fig. 8(a) and the twinned area fraction of 41% in Table 2. The twinned area fraction in this study was the ratio of the area of twins to the total observed area. The true twin thickness was calculated by multiplying the projected twin thickness measured on the observation plane with the cosine of the angle between the twinning plane (κ_1) normal and observed plane normal [22,26].

Figure 11 shows the results of Schmid factor analysis for the TTWs after 10% strain. Similar to slip, the m_{nor} was used to assess the closeness between activated m and maximum m of the six theoretical twin variants. As seen in Fig. 11(a), the V1 variants were predominant and the V6 variants had the lowest frequency. The distribution of m

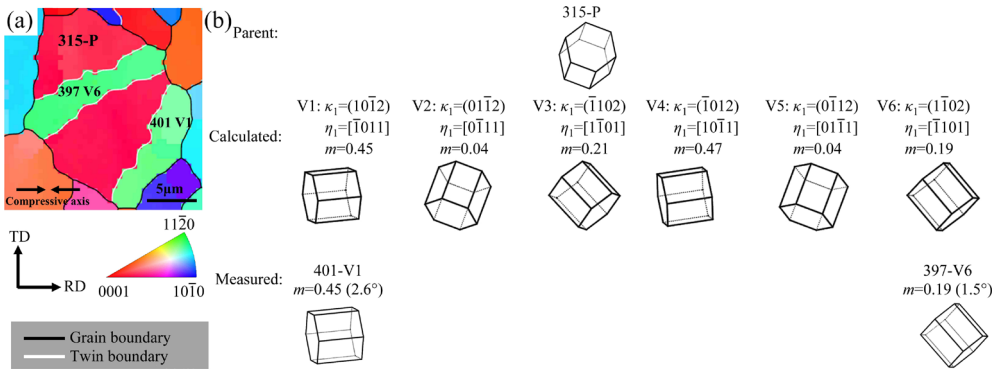

Fig. 9 Illustration of twin variants identification procedure in Grain 315: (a) IPF map of Grain 315-P containing two twins; (b) Parent grain orientation, calculated twin variants containing crystallographic orientation, and measured twin variants orientation

Table 2 Statistical information of twinning activity at 10% strain

Type	Feature	Number
Area information	Number of grains	410
	Number of grain boundaries	954
Twin information	Number of twins	363
	Average twin number per grain	0.89
	Twinned area fraction	0.41
	Number of twinned grains	225
	Twinned grain fraction (Grains with at least one twin/total grains)	0.55
	Twinned grain boundary fraction (Boundaries connected to at least one twin/total boundaries)	0.89

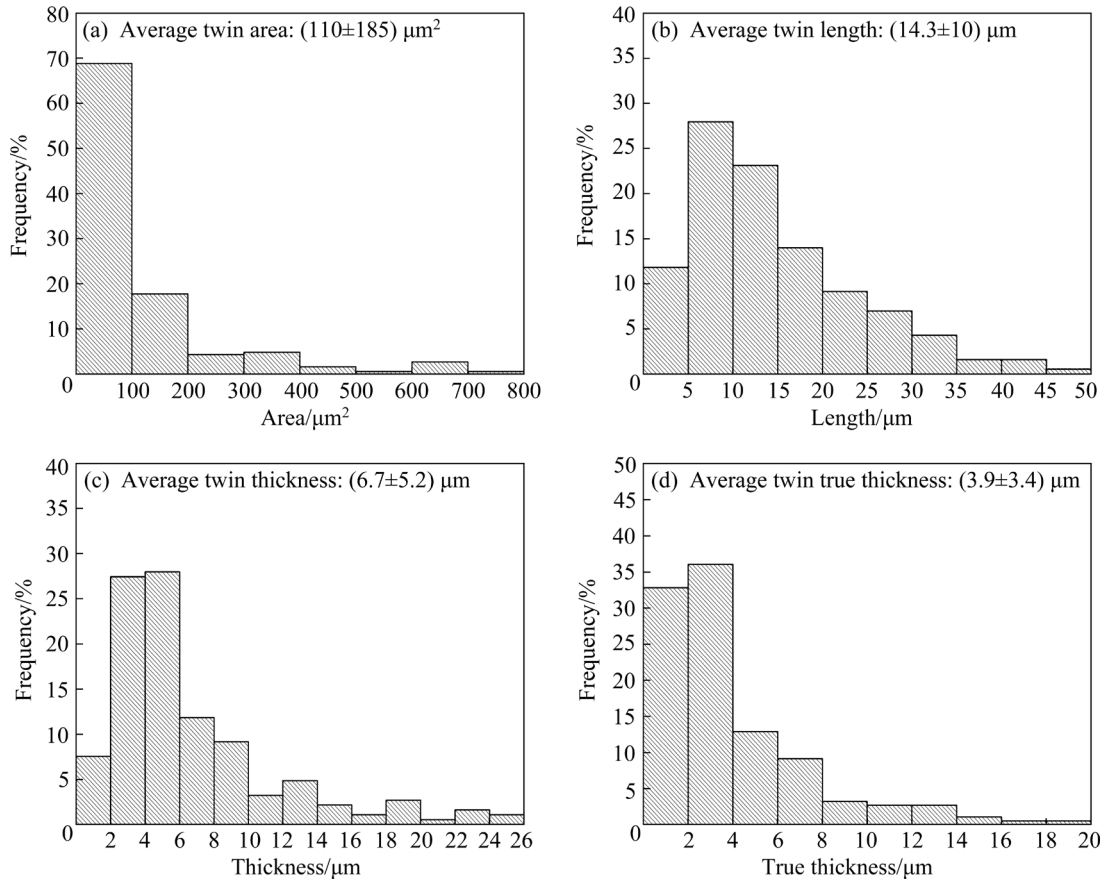

Fig. 10 Statistical information for all identified TTWs: (a) Area; (b) Length; (c) Thickness; (d) True thickness

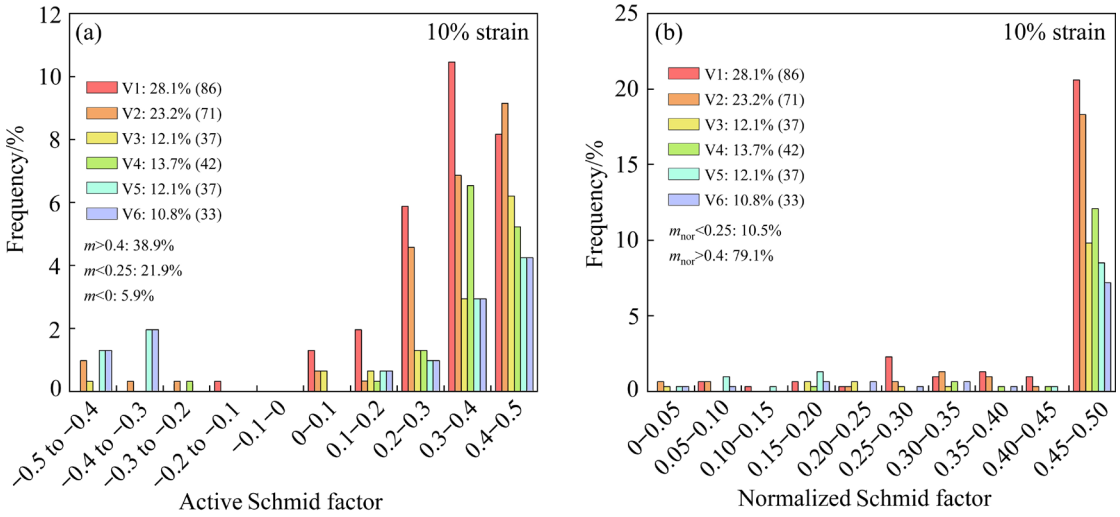

Fig. 11 Schmid factor distribution for each variant of all TTWs: (a) Schmid factor (m); (b) Normalized Schmid factor (m_{nor})

ranged from −0.5 to 0.5, with only 38.9% of the m values larger than 0.4. However, 5.9% of them exhibited negative values. The Schmid factor was calculated by assuming that the local (grain scale) stress was consistent with the global stress. Thus, the Schmid factor used in the present work is totally geometric. After normalization (Fig. 11(b)), most of the activated twin variants (79.1%) have m_{nor} values greater than 0.4, but there were still 10.5% of them showed lower values (m_{nor}<0.25). Thus, the activation of the twin variants exhibited non-negligible non-Schmid behavior.

When a twin growth encounters a grain boundary, it may induce nucleation and growth of another twin in the adjacent grain, which is known as twin transmission [26]. Luster−Morris parameter m' is also an important parameter for assessing twin transmission, which is calculated in agreement with Eq. (2). The normalized Luster−Morris parameter m'_{nor} was used to characterize how close m' is to m'_{max} among all 36 possible twin transmission combinations. The calculation of m'_{nor} is the same as Eq. (3).

Figure 12 shows the representative transmitted twin pairs and the related geometric parameters. For example, as shown in Figs. 12(a, b), the transmitted twin pairs were identified as 492-V1 and 506-V1, respectively. The m_{nor} values were both 0.5 and they exhibited good geometric compatibility (m'=0.97). However, the other three transmitted pairs in Figs. 12(c−h) exhibited negative m' values, indicating that m' was not correlated well to twin transmission.

Thus, the correlations between transmitted twin pairs and geometrical parameters, such as m, m_{nor}, m' and m'_{nor}, were further investigated. Figure 13 shows the analysis of m and m' for twin transmission, noting that for a transmitted twin pair, the m of the twin with the larger true thickness was defined as m_1. The 17 observed twin transmissions were statistically analyzed. As shown in Fig. 13(a), the distribution of m' was relatively scattered (from

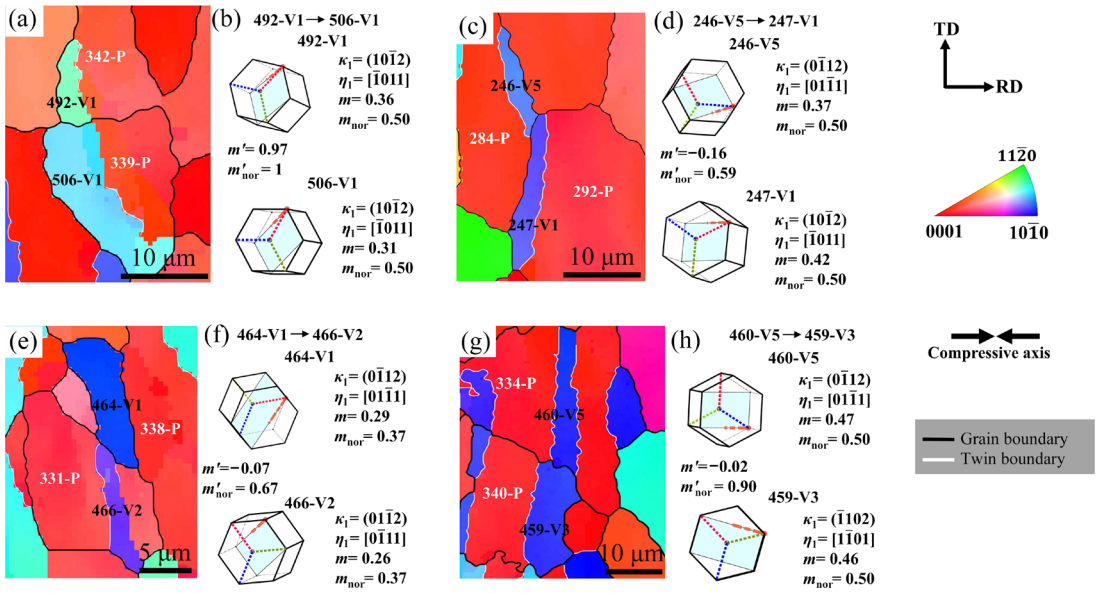

Fig. 12 Representative examples of twin transmission: (a, c, e, g) IPF maps; (b, d, f, h) Twinning plane κ_1, twinning direction η_1 and geometric parameters

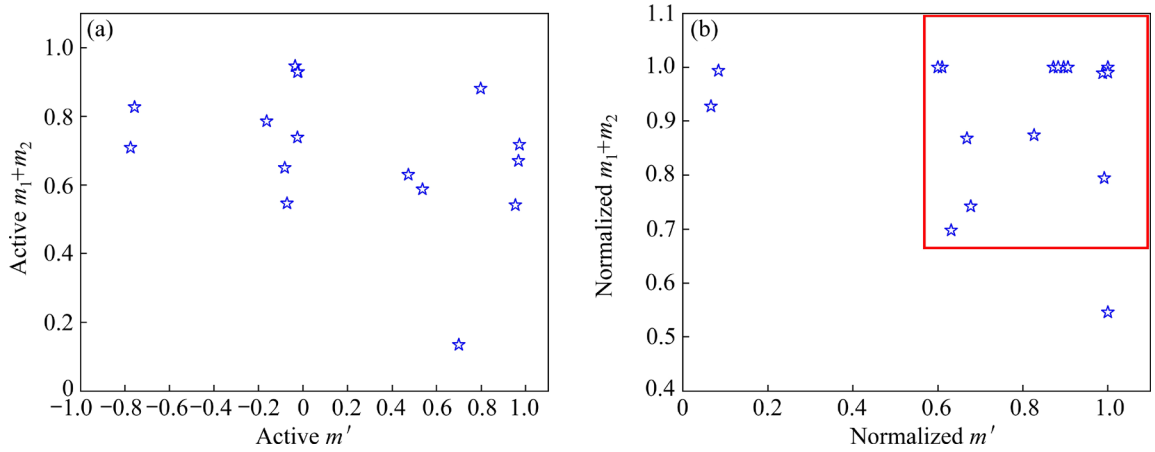

Fig. 13 Correlation between sum of Schmid factor m and Luster−Morris parameter m' for transmitted twin pairs: (a) Active; (b) Normalized

−1 to 1), with only 29% of m' values greater than 0.6 and even 59% less than 0. After normalization, a clear trend is observed in Fig. 13(b). 82% of the pairs exhibited both $m'_{nor}>0.6$ and $m_{nor1}+m_{nor2}>0.6$ (shown in the rectangle in Fig. 13(b)), revealing that twin transmission tended to exhibit large m_{nor} and m'_{nor} values.

3.6 Slip−twinning interaction

Since the twinning generally coincides with dislocation slip during deformation, the interaction between slip and twinning was inevitably observed in the present work. Figure 14 shows representative examples of the slip−twinning interactions. As shown in Figs. 14(a−d), a series of parallel slip traces were only observed in the twins (while not in the parent grains), identified as basal slip using the slip trace analysis. The information about slip systems was visualized in the unit cell. The m values of basal slip in parent grain and twin were provided in Fig. 14. Another type of interaction is presented in Figs. 14(e−h). The slip traces crossed the twin boundary straightly (slip transfer across the twin boundary), which was probably the result of another slip system being activated in the twin when the dislocation moves to the twin boundary. For example, as seen in Figs. 14(e, f), a pyramidal II-11 slip with a m value of 0.48 was induced when

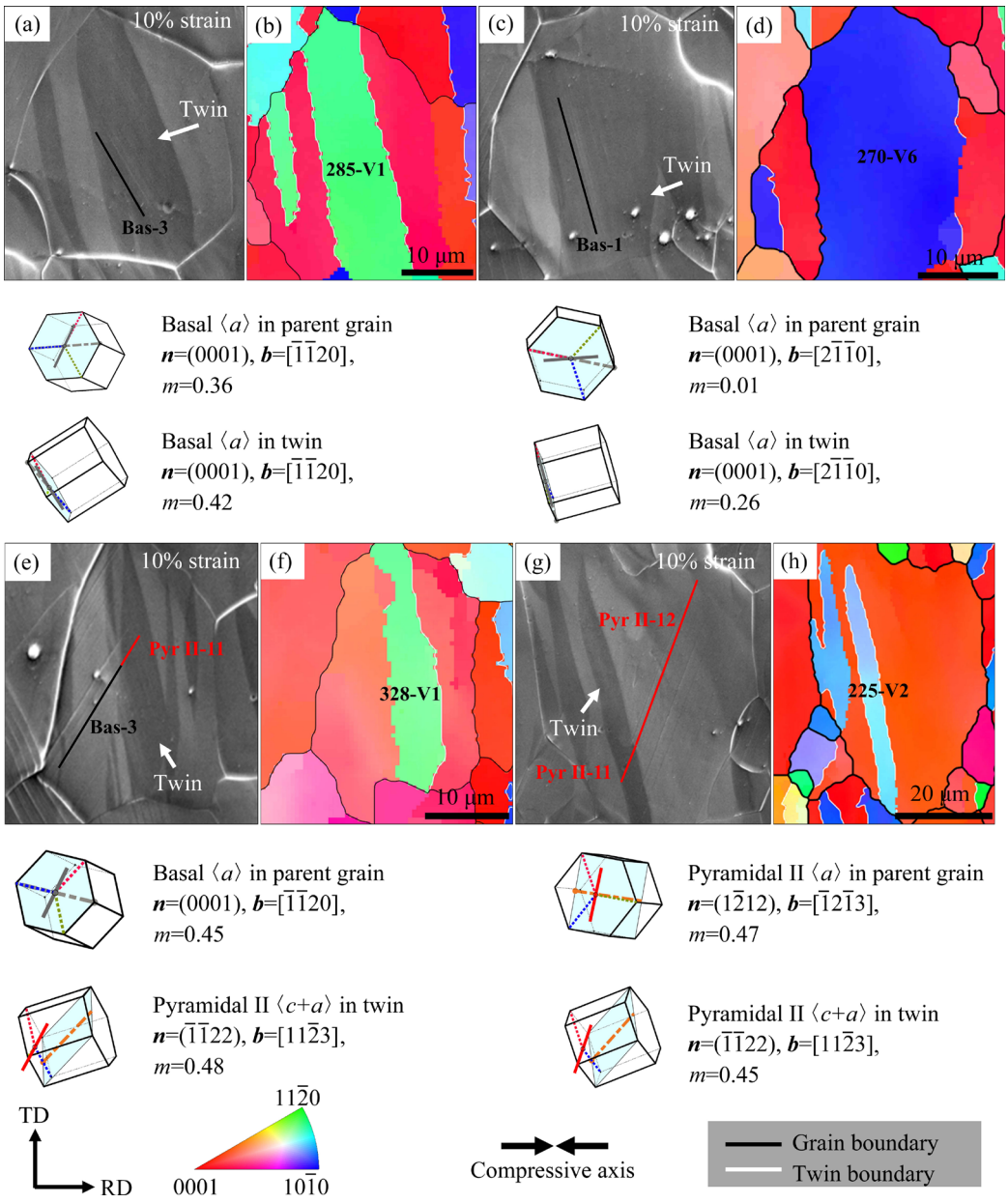

Fig. 14 Representative examples of slip−twinning interactions: (a, c, e, g) SE SEM photomicrographs; (b, d, f, h) Corresponding IPF (The slip systems and corresponding Schmid factors are given)

the bas-3 slip moved to the twin boundary. A similar case can also be seen in Figs. 14(g, h).

4 Discussion

4.1 Non-Schmid behavior of slip and twinning

As shown in Fig. 5, for basal slips, it was apparent that most of them had relatively large *m* values. Non-basal slips, however, were activated with low *m* values. The slip modes with low *m* values were also found in Mg during tension [24,28,30], Mg−3Y [22], Mg−10Y [21] and in WGZ1152 [23] during compression. It was considered that this phenomenon resulted from local stress deviating from global stress. As we know, strain accommodation among grains with different orientations can generate high stress concentrations near grain boundaries [30]. As a result, the stress state near the grain boundary may be different from the global applied stress state. The local stress triggered a deformation mechanism with a low *m* value [30], such as the pyramidal II $\langle c+a \rangle$ slip observed in this work. Furthermore, KOIKE et al [33] also showed that the activation of pyramidal $\langle c+a \rangle$ slip coordinated the deformation among grains. Therefore, the slip mode with low *m* values would be activated to keep the materials from cracking during deformation.

As shown in Fig. 11(a), the twin variant selection also exhibited non-Schmid behavior, i.e., with 21.9% of the activated *m* values less than 0.25 and 5.9% of them exhibiting negative values. CHAI et al [26] found plenty of anomalous twins in pure Mg during room temperature tension. In other words, 57% of the TTWs have *m* values less than 0. The activation of twin variants with low *m* values was also observed in HCP pure Ti during compression [34], and it was suggested that global *m* might not be a suitable characterization parameter for twin variant selection when the microstructure was highly inhomogeneous. The above phenomenon also existed in RE-alloys such as Mg−3Y [22], Mg−3Dy and Mg−3Er [35] during compression. The plastic heterogeneity, generally speaking, was responsible for the anomalous twins [22,26,34]. Many efforts have been made to understand plastic heterogeneity [21,23,26]. For example, intragranular misorientation (IGM) and geometrically necessary dislocation (GND) maps based on EBSD have been used to analyze plastic inhomogeneities in Mg [26], WGZ1152 [23] and Mg−10Y [21]. It is believed that local plastic deformation might cause a difference between the local stress state and the global stress state [26]. Similarly, in recent research on the WE43 [36] and Hastelloy X superalloy [37] alloy during tension, it was found that the local strain could even be compressive. In addition, it has been reported that twins with low *m* values could be activated through twin transmission in order to accommodate local strain [22]. What's more, the interaction of deformation mechanisms is also an important factor. The twins with low *m* values can be activated to coordinate the strain incompatibility caused by basal slip and prismatic slip [38,39]. In summary, the non-Schmid behavior of twins might be related to the microstructure [34], local stress state [26,36,37], plastic heterogeneity [21,23,26], and interaction of deformation mechanisms [38,39].

4.2 Interaction of deformation mechanism

In this section, the interactions between slip and twinning observed in this study were discussed, including slip traces within twins, the relation between the activation of twins and slip, and the slip transfer crossing the twin boundary.

As shown in Figs. 14(a−d), the basal slip traces were only activated within the twin domain, which is the most prevalent phenomenon in this study. To this end, a statistical Schmid factor analysis was performed, and the results are shown in Fig. 15. The *m* values of basal slip were larger in the twin domains than the corresponding parent grain for most of the observed cases (94%), indicating that the change in grain orientation resulting from twinning was conducive to the basal slip, which can coordinate deformation. A high-resolution TEM analysis in Mg−4Li has also shown a high density of basal slip activity within the TTW and CTW [40]. In the work of in-situ micro-compression of Mg $[2\bar{1}\bar{1}0]$ pillars [41], it was found that the TTWs activated easier when the loading axis was changed from $[2\bar{1}\bar{1}0]$ to $[11\bar{2}3]$ because of the crystal reorientation, which led to a significant increase in the *m* values of basal slip. Thus, the basal slips with high *m* values were preferred to be activated within twins. Moreover, they proposed that when the twins reached the required twin thickness for basal slip, the basal slip can also be activated within the twin.

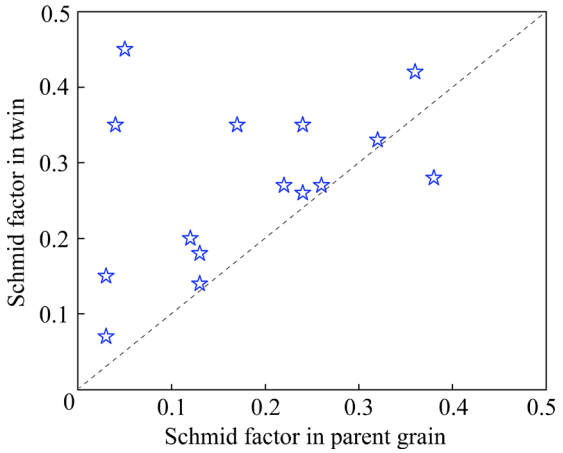

Fig. 15 Schmid factor of basal slip before and after twinning

The correlation of the twinned fraction with the maximum m value (m_{max}) of the prismatic slip in corresponding grains is shown in Fig. 16. As seen in Fig. 16, the twins were more likely to be activated in grains that favor prismatic slip. Recently, a study of the Mg−3Y deformation mechanism also reported a positive correlation between the twinned fraction and the m_{max} of the prismatic slip in the parent grain [22]. It has been demonstrated that twins were activated when a large amount of prismatic slip was needed to accommodate the strain in adjacent grains [39]. Moreover, the strain incompatibility in adjacent grains resulting from prismatic slip could be coordinated by twins. An in-situ micro-compression of Mg was performed by JEONG et al [41], and they found that the local stress concentration caused by the pile-up of prismatic $\langle a \rangle$ dislocations could provide a favorable condition for twin nucleation. Therefore, the activation of twins might be related to the prismatic slip.

Slip transfer across the twin boundary was also observed in this study, and the corresponding slip systems were identified by slip trace analysis (Figs. 14(e−h)). YOO and WEI [42] have studied the interaction between dislocation slip and twin boundary in Zn, and they have defined two kinds of slip transfers. The first is the direct slip transfer in which is a basal pure screw dislocation with a Burgers vector parallel to the twin plane cross slip from the basal plane in the parent grain to the basal plane in the twin. The second is the indirect slip transfer in which the mixed basal dislocation would be transformed into $\langle c+a \rangle$ dislocations upon incorporation into the twin [16,42]. This was similar to the observations in Fig. 14(e). The authors also observed slip transfer across the twin boundaries and concluded that an indirect slip transfer occurred. In addition, this phenomenon was interpreted as direct slip transfer in Mg [16]. TOMSETT and BEVIS [43] investigated basal slip and $\{10\bar{1}2\}$ twin boundaries by TEM, and they found that both direct and indirect slip transfer occurred in Zn.

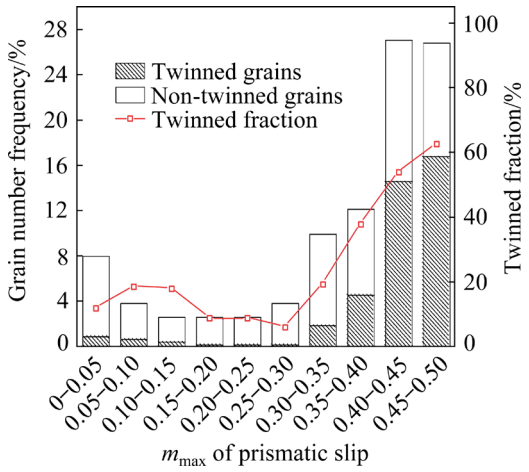

Fig. 16 Correlation of twinned fraction with m_{max} of prismatic slip in corresponding grains

5 Conclusions

(1) For 10% strain, the slip mode was dominated by basal $\langle a \rangle$ slip (89%), followed by prismatic $\langle a \rangle$ slip and pyramidal II $\langle c+a \rangle$ slip, both with a frequency of 5.5%. After normalization, 60% of the non-basal slips had m_{nor}<0.2, indicating that the activated non-basal slips exhibited no-Schmid behavior.

(2) A total of 363 twins were observed at 10% strain, and all of them were identified as TTWs. The twinned area fraction was 41%. The distribution of normalized m suggested that most twin variants (79%) followed the Schmid law.

(3) The 17 pairs of twin transmissions were observed. The Luster−Morris parameter m' did not correlate well to twin transmission. However, most twin transmissions (82%) tended to exhibit large normalized m and m'.

(4) Additional slip systems were frequently observed to be activated in twin domains while not in the parent grains because the m values of basal slip were larger in the twin domains than the

corresponding parent grain for most of the observed cases (94%). Slip transfer across twin boundaries was also observed. Statistical Schmid factor analysis indicated that the twins were more likely to be activated in grains favoring prismatic slip, revealing that twinning activity was closely related to prismatic slip.

Acknowledgments

This work was supported by the National Natural Science Foundation of China (Nos. 52171125, 52071178), the Open Testing Funding of Large Instruments and Equipment of Southwest Jiaotong University, China (No. 2022SRII-003), and the Open Funding of International Joint Laboratory for Light Alloys (MOE), Chongqing University, China. We would like to thank the Analytical and Testing Center of Southwest Jiaotong University (China) for assistance with SEM and EBSD characterization.

Data availability

The raw/processed data required to reproduce these findings are available from the corresponding author upon reasonable request.

References

[1] LI Zi-han, ZHOU Guo-wei, LI Da-yong, WANG Hua-miao, TANG Wei-qin, PENG Ying-hong, ZUROB H S, WU Pei-dong. Crystal plasticity based modeling of grain boundary sliding in magnesium alloy AZ31B sheet [J]. Transactions of Nonferrous Metals Society of China, 2021, 31(1): 138−155.

[2] ZHANG Zhi, ZHANG Jing-huai, XIE Jin-shu, LIU Shu-juan, HE Yu-ying, GUAN Kai, WU Rui-zhi. Developing a low-alloyed fine-grained Mg alloy with high strength−ductility based on dislocation evolution and grain boundary segregation [J]. Scripta Materialia, 2022, 209: 114414.

[3] FENG Li, ZHANG You-wei, WEN Chen, LI Si-zhen, LI Jia-feng, CHENG De, BAI Jing-ying, CUI Qing-xin, ZHANG Li-gong. Effect of initial deposition behavior on properties of electroless Ni−P coating on ZK60 and ME20 magnesium alloys [J]. Transactions of Nonferrous Metals Society of China, 2021, 31(8): 2307−2322.

[4] LU Li-wei, LIU Xiao-ye, SHI Dong-feng, MA Min, WANG Zhong-chang. Effect of twinning behavior on dynamic recrystallization during extrusion of AZ31 Mg alloy [J]. JOM, 2019, 71(4): 1566−1573.

[5] LIU Xiao-ye, LU Li-wei, SHENG Kun, ZHOU Tao. Microstructure and texture evolution during the direct extrusion and bending−shear deformation of AZ31 magnesium alloy [J]. Acta Metallurgica Sinica (English Letters), 2019, 32(6): 710−718.

[6] ZHANG Zhi, ZHANG Jing-huai, XIE Jin-shu, LIU Shu-juan, HE Yu-ying, WANG Ru, FANG Da-qing, FU Wei, JIAO Yun-lei, WU Rui-zhi. Significantly enhanced grain boundary Zn and Ca co-segregation of dilute Mg alloy via trace Sm addition [J]. Materials Science and Engineering A, 2022, 831: 142259.

[7] SHENG Kun, LU Li-wei, XIANG Yao, MA Min, WU Zhi-qiang. Crack behavior in Mg/Al alloy thin sheet during hot compound extrusion [J]. Journal of Magnesium and Alloys, 2019, 7(4): 717−724.

[8] WEI Kang, XIAO Li-rong, GAO Bo, LI Lei, LIU Yi, DING Zhi-gang, LIU Wei, ZHOU Hao, ZHAO Yong-hao. Enhancing the strain hardening and ductility of Mg−Y alloy by introducing stacking faults [J]. Journal of Magnesium and Alloys, 2020, 8(4): 1221−1227.

[9] YANG Wu, QUAN Gao-feng, JI Bin, WAN You-fu, ZHOU Hao, ZHENG Jiang, YIN Dong-di. Effect of Y content and equal channel angular pressing on the microstructure, texture and mechanical property of extruded Mg−Y alloys [J]. Journal of Magnesium and Alloys, 2022, 10(1):195−208.

[10] YOO M H. Slip, twinning, and fracture in hexagonal close-packed metals [J]. Metallurgical Transactions A, 1981, 12(3): 409−418.

[11] YIN Dong-di, WANG Qu-dong, BOEHLERT C J, CHEN Zhe, LI Hong-mei, MISHRA R K, CHAKKEDATH A. In situ study of the tensile deformation and fracture modes in peak-aged cast Mg−11Y−5Gd−2Zn−0.5Zr (weight percent) [J]. Metallurgical and Materials Transactions A, 2016, 12(47): 6438−6452.

[12] TANG Xiao-zhi, ZHANG Hui-shi, GUO Ya-fang. Atomistic simulations of interactions between screw dislocation and twin boundaries in zirconium [J]. Transactions of Nonferrous Metals Society of China, 2018, 28(6): 1192−1199.

[13] QIAN Qi, LIU Zheng-qing, JIANG Yong, WANG Yi-ren, AN Xing-long, SONG Min. Basal stacking fault induced twin boundary gliding, twinning disconnection and twin growth in hcp Ti from the first-principles [J]. Transactions of Nonferrous Metals Society of China, 2021, 31(2): 382−390.

[14] XU Hong-lu, SU Xiao-ming, YUAN Guang-yin, JIN Zhao-hui. Primary and secondary modes of deformation twinning in HCP Mg based on atomistic simulations [J]. Transactions of Nonferrous Metals Society of China, 2014, 24(12): 3804−3809.

[15] AGNEW S R, DUYGULU Ö. Plastic anisotropy and the role of non-basal slip in magnesium alloy AZ31B [J]. International Journal of Plasticity, 2005, 21(6): 1161−1193.

[16] MOLODOV K D, AL-SAMMAN T, MOLODOV D A. Profuse slip transmission across twin boundaries in magnesium [J]. Acta Materialia, 2017, 124: 397−409.

[17] ZHAO De-xin, MA Xiao-long, SRIVASTAVA A, TURNER G, KARAMAN I, XIE K Y. Significant disparity of non-basal dislocation activities in hot-rolled highly-textured Mg and Mg−3Al−1Zn alloy under tension [J]. Acta Materialia, 2021, 207: 116691.

[18] MIURA S, IMAGAWA S, TOYODA T, OHKUBO K, MOHRI T. Effect of rare-earth elements Y and Dy on the deformation behavior of Mg alloy single crystals [J]. Materials Transactions, 2008, 49(5): 952−956.

[19] ZHANG Zhen, PENG Jin-hua, HUANG Ji-an, GUO Peng, LIU Zhao, SONG Shi-chao, WANG Yu. {10$\bar{1}$2} twinning nucleation in magnesium assisted by alternative sweeping of partial dislocations via an intermediate precursor [J]. Journal of Magnesium and Alloys, 2020, 8(4): 1102−1108.

[20] DI GIOACCHINO F, DA FONSECA, J Q. An experimental study of the polycrystalline plasticity of austenitic stainless steel [J]. International Journal of Plasticity, 2015, 74: 92−109.

[21] NI Ran, JIANG Zhi-wei, YIN Dong-di, YANG Wu, ZHOU Hao, ZHENG Jiang, WANG Qu-dong. Investigation on slip activity and plastic heterogeneity of aged Mg−10Y sheets during compression [J]. Metallurgical and Materials Transactions A, 2022, 53: 535−555.

[22] HUA Shen, JIANG Zhi-wei, WAN You-fu, HUANG Guang-hao, ZHOU Hao, ZHENG Jiang, WANG Qu-dong, YIN Dong-di. A statistical analysis of compressive deformation mechanisms in an extruded Mg−3Y sheet [J]. Materials Science and Engineering A, 2021, 825: 141927.

[23] NI Ran, MA Shi-jun, LONG Li-jun, ZHENG Jiang, ZHOU Hao, WANG Qu-dong, YIN Dong-di. Effects of precipitate on the slip activity and plastic heterogeneity of Mg−11Y−5Gd−2Zn−0.5Zr (wt.%) during room temperature compression [J]. Materials Science and Engineering A, 2021, 804: 140738.

[24] YIN Dong-di, BOEHLERT C J, LONG Li-jun, HUANG Guang-hao, ZHOU Hao, ZHENG Jiang, WANG Qu-dong. Tension−compression asymmetry and the underlying slip/twinning activity in extruded Mg−Y sheets [J]. International Journal of Plasticity, 2021, 136: 102878.

[25] LONG Li-jun, HUANG Guang-hao, YIN Dong-di, JI Bin, ZHOU Hao, WANG Qu-dong. Effects of Y on the deformation mechanisms of extruded Mg−Y sheets during room-temperature compression [J]. Metallurgical and Materials Transactions A, 2020, 51: 2738−2751.

[26] CHAI Yan-qin, BOEHLERT C J, WAN You-fu, HUANG Guang-hao, ZHOU Hao, ZHENG Jiang, WANG Qu-dong, YIN Dong-di. Anomalous tension twinning activity in extruded Mg sheet during hard-orientation loading at room temperature [J]. Metallurgical and Materials Transactions A, 2021, 52: 449−456.

[27] BEYERLEIN I J, CAPOLUNGO L, MARSHALL P E, MCCABE R J, TOMÉ C N. Statistical analyses of deformation twinning in magnesium [J]. Philosophical Magazine, 2010, 90(16): 2161−2190.

[28] CEPEDA-JIMÉNEZ C M, MOLINA-ALDAREGUIA J M, CARREÑO F, PÉREZ-PRADO M T. Prominent role of basal slip during high-temperature deformation of pure Mg polycrystals [J]. Acta Materialia, 2015, 85: 1−13.

[29] CEPEDA-JIMÉNEZ C M, MOLINA-ALDAREGUIA J M, PÉREZ-PRADO M T. Origin of the twinning to slip transition with grain size refinement, with decreasing strain rate and with increasing temperature in magnesium [J]. Acta Materialia, 2015, 88: 232−244.

[30] CEPEDA-JIMÉNEZ C M, MOLINA-ALDAREGUIA J M, PÉREZ-PRADO M T. Effect of grain size on slip activity in pure magnesium polycrystals [J]. Acta Materialia, 2015, 84: 443−456.

[31] HABIB S A, KHAN A S, GNÄUPEL-HEROLD T, LLOYD J T, SCHOENFELD S E. Anisotropy, tension−compression asymmetry and texture evolution of a rare-earth-containing magnesium alloy sheet, ZEK100, at different strain rates and temperatures: Experiments and modeling [J]. International Journal of Plasticity, 2017, 95: 163−190.

[32] BACHMANN F, HIELSCHER R, SCHAEBEN H. Texture analysis with MTEX-free and open source software toolbox [J]. Solid State Phenomena, 2010, 160: 63−68.

[33] KOIKE J, KOBAYASHI T, MUKAI T, WATANABE H, SUZUKI M, MARUYAMA K, HIGASHI K. The activity of non-basal slip systems and dynamic recovery at room temperature in fine-grained AZ31B magnesium alloys [J]. Acta Materialia, 2003, 51: 2055−2065.

[34] ARUL KUMAR M, WROŃSKI M, MCCABE R J, CAPOLUNGO L, WIERZBANOWSKI K, TOMÉ C N. Role of microstructure on twin nucleation and growth in HCP titanium: A statistical study [J]. Acta Materialia, 2018, 148: 123−132.

[35] WANG F, SANDLÖBES S, DIEHL M, SHARMA L, ROTERS F, RAABE D. In situ observation of collective grain-scale mechanics in Mg and Mg−rare earth alloys [J]. Acta Materialia, 2014, 80: 77−93.

[36] GITHENS A, GANESAN S, CHEN Z, ALLISON J, SUNDARARAGHAVAN V, DALY S. Characterizing microscale deformation mechanisms and macroscopic tensile properties of a high strength magnesium rare-earth alloy: A combined experimental and crystal plasticity approach [J]. Acta Materialia, 2020, 186: 77−94.

[37] ABUZAID W Z, SANGID M D, CARROLL J D, SEHITOGLU H, LAMBROS J. Slip transfer and plastic strain accumulation across grain boundaries in Hastelloy X [J]. Journal of the Mechanics and Physics of Solids, 2012, 60(6): 1201−1220.

[38] KOIKE J, SATO Y, ANDO D. Origin of the anomalous {10$\bar{1}$2} twinning during tensile deformation of Mg alloy Sheet [J]. Materials Transactions, 2008, 49(12): 2792−2800.

[39] JONAS J J, MU S, AL-SAMMAN T, GOTTSTEIN G, JIANG L, MARTIN É. The role of strain accommodation during the variant selection of primary twins in magnesium [J]. Acta Materialia, 2011, 59: 2046−2056.

[40] LENTZ M, COELHO R S, CAMIN B, FAHRENSON C, SCHAEFER N, SELVE S, LINK T, BEYERLEIN I J, REIMERS W. In-situ, ex-situ EBSD and (HR-)TEM analyses of primary, secondary and tertiary twin development in an Mg−4wt.%Li alloy [J]. Materials Science and Engineering A, 2014, 610: 54−64.

[41] JEONG J, ALFREIDER M, KONETSCHNIK R, KIENER D, OH S H. In-situ TEM observation of {10$\bar{1}$2} twin-dominated deformation of Mg pillars: Twinning mechanism, size effects and rate dependency [J]. Acta Materialia, 2018, 158: 407−421.

[42] YOO M H, WEI C T. Growth of deformation twins in zinc crystals [J]. Philosophical Magazine, 1966, 14(129): 573−587.

[43] TOMSETT D I, BEVIS M. The incorporation of basal slip dislocations in {10$\bar{1}$2} twins in zinc crystals [J]. Philosophical Magazine, 1969, 19(157): 129−140.

轧制纯 Mg 板材压缩变形机制的统计研究

尹冬弟[1]，陈 波[1]，柴艳琴[1]，万有富[1]，周 浩[2]，郑 江[3]，王渠东[4]，曾 迎[1]

1. 西南交通大学 材料科学与工程学院 材料先进技术教育部重点实验室，成都 610031；
2. 南京理工大学 材料科学与工程学院 纳米异构材料中心，南京 210094；
3. 重庆大学 沈阳材料科学国家研究中心轻金属材料研究部
材料科学与工程学院 教育部轻合金材料国际合作联合实验室，重庆 400044；
4. 上海交通大学 材料科学与工程学院 轻合金精密成型国家工程研究中心，上海 200240

摘 要：基于 EBSD 和滑移迹线分析，在晶粒尺度上对轧制纯镁板材室温压缩过程中的滑移/孪生激活规律以及他们之间的交互作用进行统计研究(~400 个晶粒)。10%变形后的结果表明，基面滑移(89%)是主要的滑移模式，所有鉴别出来的 363 个孪晶为拉伸孪晶。上凹形的应力−应变曲线表明变形由孪生主导，高的孪生面积分数(41%)进一步验证上述结论。大多数孪晶变体(79%)遵循施密特定律，孪晶转移与 Luster−Morris 参数(m')并没有很好的相关性，然而大多数孪晶转移(82%)表现出较大的归一化施密特因子(m)和 m'值。在孪晶内观察到滑移系的激活且符合施密特定律。此外，还观察到滑移迹线穿过孪晶界的现象。对 m 统计分析表明，孪生激活与柱面滑移密切相关。

关键词：镁；EBSD；滑移迹线分析；孪晶变体选择；滑移−孪生交互作用

(Edited by Bing YANG)